

Article

Dynamic Response and Failure Process of a Counter-Bedding Rock Slope under Strong Earthquake Conditions

Ming-Zhu Guo, Kun-Sheng Gu  and Chen Wang 

Department of Urban Construction, Beijing University of Technology, Beijing 100124, China; gmsz@bjut.edu.cn (M.-Z.G.); 1422896940@emails.bjut.edu.cn (C.W.)

* Correspondence: guks@emails.bjut.edu.cn

Abstract: There are massive landslides and potential landslides along the Three Rivers Basin in the Qinghai–Tibet Plateau, which pose a serious threat to the Sichuan–Tibet Railway. A normal shaking table model test was conducted to study the dynamic characteristics and dynamic response of a symmetrical counter-bedding rock slope based on the Zongrong Village landslide. The influences of the dynamic parameters, seismic wave type, and a weak intercalated layer on the slope’s dynamic response were considered. The results showed symmetry between the growth trend of the acceleration amplification factor and other research results. When the input wave amplitude was constant, the acceleration amplification factor increased at first and then decreased as the frequency increased. When the input frequency was near the slope’s natural frequency, the acceleration amplification factor increased at first and then decreased with an increase in the input amplitude and reached the maximum value at 0.3 g. The acceleration amplification factor increased linearly with height in the vertical direction inside the slope but increased slowly at first and then sharply along the slope surface, reaching the maximum value at the slope’s top and exhibiting an obvious “elevation effect”. When sinusoidal waves, Wolong waves, and Maoxian waves with the same amplitude were input, the slope’s amplification effect on the bedrock wave was more obvious. The weak intercalated layer showed the phenomenon of “thin layer amplification” and “thick layer attenuation” in response to the input seismic wave. The slope’s failure process can be roughly divided into three stages: (1) the formation of tensile cracks at the top and shear cracks at the toe; (2) the extension of cracks and the sliding of the slope-surface block; (3) the formation of the main sliding surface.

Keywords: shaking table test; counter-bedding rock slope; dynamic response; instability failure process



Citation: Guo, M.-Z.; Gu, K.-S.; Wang, C. Dynamic Response and Failure Process of a Counter-Bedding Rock Slope under Strong Earthquake Conditions. *Symmetry* **2022**, *14*, 103. <https://doi.org/10.3390/sym14010103>

Academic Editor: Hari M. Srivastava

Received: 29 November 2021

Accepted: 5 January 2022

Published: 7 January 2022

Publisher’s Note: MDPI stays neutral with regard to jurisdictional claims in published maps and institutional affiliations.



Copyright: © 2022 by the authors. Licensee MDPI, Basel, Switzerland. This article is an open access article distributed under the terms and conditions of the Creative Commons Attribution (CC BY) license (<https://creativecommons.org/licenses/by/4.0/>).

1. Introduction

The Three Rivers Basin, which spans the deeply incised southeast Tibetan Plateau and north Tibetan Plateau, is characterised by highly varied topography and climate, strong neotectonic movement, and frequent seismicity, resulting in frequent geological disasters [1]. This poses a severe threat to people’s lives and properties and to the regular operation of important infrastructure projects. Earthquakes, one of the important dynamic factors in inducing landslides, have an extensive trigger range which can result in widespread disaster [2]. For example, in the occurrence of the Wenchuan earthquake in 2008, more than 48,000 landslides were triggered, causing approximately 20,000 deaths [3,4]. In terms of the types of landslides, bedded rock slopes account for 60% of landslides [5]. As a type of layered rock slope, the counter-bedding slope is considered relatively stable in traditional engineering geology research. However, with the increase in engineering activities, a mass of counter-bedding-slope-instability failure cases have appeared at home and abroad [6], such as the Xuelongnang landslide [7] and the Daguangbao giant landslide [8]. Therefore, the construction of the Sichuan–Tibet Railway is a significant opportunity to study the typical counter-bedding slope in the Three Rivers Basin of the Qinghai–Tibet Plateau.

In recent years, many scholars have researched slope dynamic responses and failure mechanisms, mainly focusing on field investigations, numerical simulations, and physical model tests. Some scholars have found that the dynamic amplification effect at the ridge is significantly higher than that at the toe of the slope by analysing the data obtained from field monitoring, which presented an apparent topographic amplification effect [9–11]. However, with the same elevation and different depths of a slope, the closer to the slope surface, the more obvious the acceleration amplification effect [12,13]. Other scholars have analysed the effect of the lithology and structure plane on the dynamic amplification of slopes and pointed out that the lithology and structural plane significantly affect the slopes' dynamic responses and failure processes [14–16]. However, earthquakes are random, which leads to uncertainty in the results of the monitoring. Therefore, numerical simulation has gradually turned into a crucial method for studying a slope's dynamic response and stability. Some scholars have used different numerical calculation methods [17,18] to analyse the influence of ground motion parameters on a slope's dynamic response. Song et al. [19] studied the relationship between the local damage and the dynamic failure of a rock slope with discontinuous joints and its failure mechanism in the frequency domain. In the second year [20], they analysed the effect of the rock mass structure and lithology on a slope's dynamic response, finding that the amplification effect of soft rock on ground motion is higher than that of hard rock, and that the amplification effect of layered rock slopes is higher than that of homogeneous slopes. Feng et al. [21] used a discontinuous deformation analysis method and shaking table test to analyse the dynamic response and the failure process of a layered rock slope. Mao et al. [22] used ANSYS to analyse the slopes' deformation and failure characteristics under the action of common and rare earthquakes.

In addition to the research methods mentioned above, a physical model experiment, as an intuitive observation of the slope failure process, has the advantage of repeatability and has been applied by some researchers. Zhao et al. [23] studied the dynamic response of a slope under a random earthquake from the time domain and space domain by a shaking table test. Srilatha et al. [24] studied the influence of the input wave frequency on the dynamic response of reinforced and unreinforced slopes by a shaking table test and pointed out that the dynamic responses of slopes did not increase linearly with the increase in input wave frequency. Feng et al. [25–27] analysed the effect of frequency on the slope's dynamic response by using a shaking table test, finding that the slope's acceleration amplification factor rises with the increase in frequency and becomes more apparent when the frequency of the input wave is close to the slope's natural frequency. However, the frequency of the input waves do not exceed the slope's natural frequency. Chen et al. [28] studied the dynamic response and failure process of the anti-dip rock slope by a shaking table test and found that the damage of low-frequency and high-amplitude seismic waves to the slope is higher. Liu et al. [29,30] discussed the influence of the direction of the input seismic wave on the slope's dynamic response and pointed out that the horizontal-acceleration amplification effect is higher than that for the vertical acceleration. Chen et al. [31] studied the influence of the thickness and angle of a weak intercalated layer on a slope's dynamic response and pointed out that the existence of a weak intercalated layer reduces the slope's stability. Li et al. [32] analysed a counter-bedding rock slope's dynamic response with multiple slip surfaces, considering the effect of slope height, slope angle, and input seismic wave on the slope's critical acceleration. He et al. [33] found that the slope begins to exhibit a nonlinear dynamic response when the amplitude of the input wave exceeds 0.2 g, and that the existence of a structural plane affects the distribution of horizontal seismic waves. Lin et al. [34,35] analysed the linear and nonlinear behavior of slopes; however, the input amplitudes of seismic waves are different when the slope presents nonlinear variations. Li et al. [36] compared and analysed the dynamic responses of bedding slopes and anti-dip rock slopes by using a shaking table test. The results indicated that the failure modes are very different between the bedding rock slope and anti-dip rock slope. Deng et al. [37] studied a slope's dynamic stability under earthquakes by using different research methods, considering the influence of slope height, slope angle, rock-layer dip angle, and thickness.

Wang et al. [38] analysed the change in the displacement of measuring points on a slope surface through a shaking table test and gave the judgment basis for slope crack initiation and instability.

Besides a shaking table test, a centrifuge model test can be used to study the failure modes of weak–hard interbedded slopes. Huang et al. [39,40] carried out research about the difference in failure modes between a single-layered rock slope and an interbedded counter-bedding rock slope with different layer thickness ratios of soft rock and hard rock. Li et al. [41] studied the deformation characteristics of a counter-bedding slope with soft and hard interbedded layers by a centrifuge test and numerical simulation. Li et al. [42] studied the failure mode of a slope during impoundment by a centrifuge test and numerical simulation, and pointed out that the initial phase of water-level rise is likely the most dangerous phase with respect to soil slope stability.

As an important part of a slope, interstitial water has a great influence on the stability of a slope. Paster [43] established a depth integral model based on the Biot–Zienkiewicz equations in the mathematical model, combining the depth integral description of a soil-pore fluid mixture with a set of 1D models to deal with the evolution of pore pressure in soil. Paster [44] applied the depth integral model considering pore-water-pressure dissipation to landslide collapse. Kakogiannou [45] used the finite element model for coupled elasto-plastic variably-saturated porous geomaterials and gives three different criterion expressions to simulate the local and diffusion failure modes of the soil. By analyzing the natural rock collapse events, Sosio [46] performed a quasi-3D continuum dynamic analysis of the landslide motion, assuming both a Voellmy and a frictional rheological in the model DAN 3D.

The purpose of this paper is to study the dynamic response law of a rock slope under a strong earthquake. Due to the limitations of the model box and test conditions, interstitial water is not the main consideration factor. Besides, the above studies show that the input ground motion parameters and structure planes greatly influence a slope's dynamic response and failure mechanism. However, most of the input frequencies are lower than the slope's natural frequency. In regard to the seismic waves input scheme of the rock slope, the soil waves and sinusoidal waves were mostly selected, with few studies considering the input of bedrock seismic waves. This study takes a counter-bedding rock slope as the prototype, which is located in the Three Rivers Basin of the southeastern Tibetan Plateau, adjacent to Zongrong Village. A shaking table test was conducted to study the slope's dynamic response and failure processes according to the similarity theory. The effects of the dynamic slope response on different types of ground motion parameters and the seismic wave type and weak interlayer were considered. The research results help greatly in our understanding of the effect of seismic waves on slopes' dynamic responses, as well as contributing to further discussion on slopes' failure mechanisms and to the prevention of disasters.

2. Geological Conditions of the Landslide Area

The Zongrong Village landslide is located 82 km upstream of the Jinsha River in Benzilan Town, on the left bank of the Jinsha River. The geological survey shows that the landslide is in the shape of an armchair, with a leading-edge elevation of 2145 m and a trailing-edge elevation of 2920 m. The left and right sides of the landslide each have a large gully, with the right having a blunt face towards Xu Long Township and the left gully facing Zongrong Village. The back wall of the landslide is steep, and the middle part of the landslide is gentle. The landslide front is a steep slope which is the shear outlet of the dumping deformation. The landslide area is shown in Figure 1.

There are six lithology types in the study area: (1) Q_{h-del} landslide accumulation; (2) $Q_{h-esl+al}$ Holocene alluvial + eluvial diluvial; (3) $T_3\delta o$ quartz diorite; (4) P_2X^3 Middle Proterozoic mica gneiss; (5) D_{TJ} Palaeozoic ophiolites (amphibolites); (6) Q_4 Holocene lacustrine deposits. Most of the geological structures in the landslide area are joints and fissures. In the exposed area of the bedrock gneiss, there are obvious schistosity and

gneissosity structures, and the rock mass is mostly a layered massive structure which inclines inshore, forming a high and steep counter-bedding slope. The plan and profile of the landslide area are shown in Figure 2.

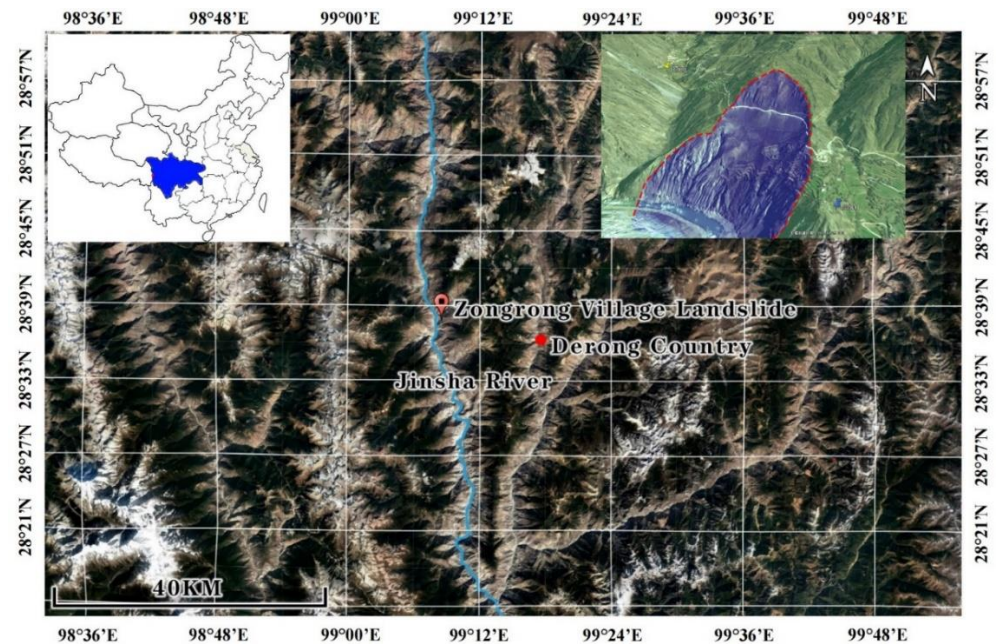


Figure 1. Location of the landslide area.

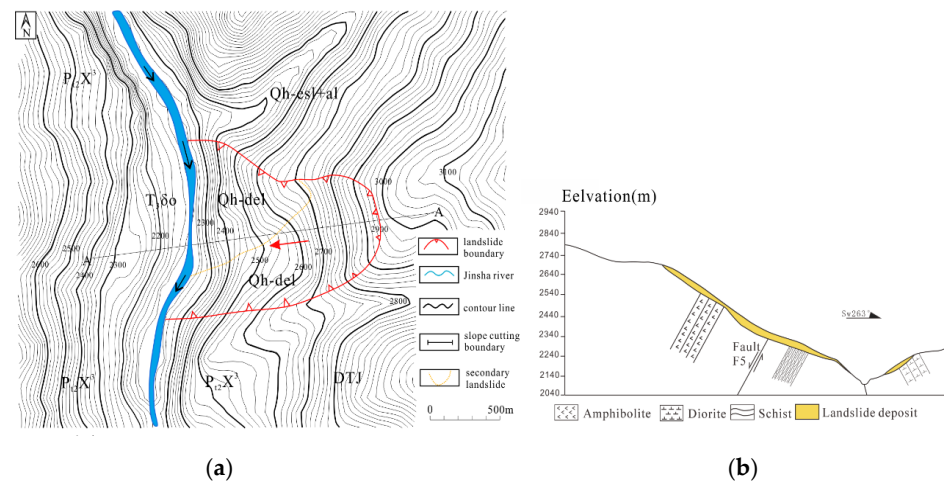


Figure 2. The landslide area: (a) planar map of Zongrong landslide; (b) sketch map of profile 'AA'.

3. Shaking Table Test

3.1. Test Equipment

The shaking table model test was performed at the Laboratory of the West District of Beijing University of Technology, China. The table showed horizontal and unidirectional loading. The shaking table size was 3 m × 3 m, and the maximum load was 10 t. The operating frequency range was 0–50 Hz, the maximum displacement in the X and Y directions was ±120 mm, and the full-load acceleration was ±1.5 g. A rigid model box with the size 2.97 m × 1.2 m × 1.52 m (length × width × height) was used in the test. The outer frame was welded with Q235 steel pipes and surrounded by acrylic plates, which made it convenient to observe the changes in the model. A rubber cushion was added between the outer frame and the acrylic plate to protect the acrylic plate. The shake table and model boxes are shown in Figure 3.

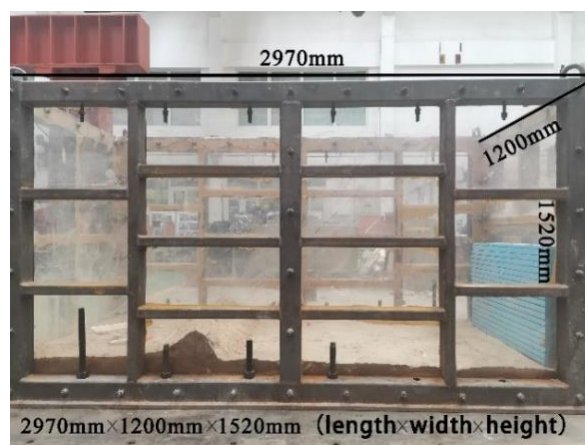


Figure 3. Test equipment and model box.

3.2. Physical Model Test

The similarity principle is a crucial premise for shaking table test research and is also the basis for creating models with similar materials [40]. Therefore, the similarity between the prototype and the model should be satisfied as much as possible. However, considering the engineering situation of the Zongrong landslide, the limitation of shaking table equipment, the size of the model box, and the limitations of related physical parameters, similar parameters could not completely meet the requirements of a similar theory. Hence, the main similarity parameters affecting the model were determined according to the research problem, similarity principle, and dimensional analysis. The geometric dimension L , density ρ , and elastic modulus E were chosen as the basic control parameters, and other similar parameters were deduced, as shown in Table 1.

Table 1. The main similarity parameters of the shaking table test.

Parameters	Definition	Reduced Scale
Length l	C_l	100 *
Density ρ	C_γ	1 *
Elastic modulus E	C_E	100 *
Cohesion φ	$C_\varphi = C_E$	100
Friction angle c	C_c	1
Poisson's ratio μ	C_μ	1
Acceleration a	C_a	1
Displacement d	C_d	100
Time t	C_t	10
Frequency f	C_f	1/10

* Basic dimensions.

3.3. Material Used

The geological survey found that the main rocks in the study area were ophiolite (hornblende), gneiss, and diorite. A point-load test was conducted on rock samples in the study area to obtain the basic physical and mechanical indexes of the three rock types in the Zongrong landslide, as shown in Table 2.

Table 2. Physical and mechanical parameters of the prototype.

Rock Types	Point-Load Strength/MPa	Compressive Strength R_c /MPa	Tensile Strength R_t /MPa	Cohesion/MPa	Friction Angle/ $^\circ$	Elastic Modulus/MPa	Poisson's Ratio	Bulk Density/ $kN \cdot m^{-2}$
Ophiolite	6.79	95.99	10.19	15.63	48.52	2384.0	0.19	28.60
Diorite	8.18	110.38	12.27	18.40	47.81	2537.2	0.19	25.35
Gneiss	6.15	89.12	9.23	13.34	38.90	1680.4	0.19	24.82

In this study, quartz sand, gypsum, water, barite, and cement were selected as raw materials to produce both rock-like and interlayer bonding materials similar to those commonly used in model tests and test ratios. The ratio of similar materials was determined by using direct shear and uniaxial compression tests. The similar material ratio of mica schist was quartz sand: gypsum: cement: water: barite = 1:0.350:0.025:0.613:1, and that of ophiolite was quartz sand: gypsum: cement: water = 1:0.6:0.050:0.4. The ratio of similar materials for interlayer bonding was quartz sand: gypsum: 2% borax aqueous solution = 1:0.45:0.4. The mechanical parameters of similar materials obtained through indoor physical tests are listed in Table 3.

Table 3. Physical and mechanical parameters of the model.

Item	Density $\rho/\text{kN}\cdot\text{m}^{-2}$	Elastic Modulus E/Mpa	Cohesion ϕ/Mpa	Friction Angle c	Poisson's Ratio μ
Hardrock	26.98	20.57	0.18	44.52	0.23
Soft rock	24.82	12.68	0.12 <td>35.6</td> <td>0.19</td>	35.6	0.19

3.4. Model Design

Based on the above similarity relation, the size of the model test was 2600 mm × 1100 mm × 1300 mm (length × width × height). For the convenience of model building, the joint dip angle was designed to be 50°, and the slope angle was 45°. Two blocks with different material ratios were used to simulate the two lithologies of the Zongrong landslide. The ophiolite test block was made of gypsum board with a size of 240 mm × 120 mm × 9 mm (length × width × height), and the gneiss test block was made of paper gypsum with the same size as the ophiolite test block. Paper gypsum can also be used to simulate the interlayer joints of a counter-bedding rock slope. A mortar and gypsum mixture was used to simulate the weak intercalated layer between the lithologic interface. To mirror the actual situation, a weak interlayer with a thin bottom and a thick top was adopted. The model design is illustrated in Figure 4a. To reduce the effect of the “model box effect” on the experiment process, a polyethylene foam board with 100 mm thickness was placed between the back edge of the test model and the acrylic board. To ensure the integrity of the layer, staggered joints were used for stacking model masonry, and the masonry direction was from the toe to the slope’s back edge. A model masonry drawing is shown in Figure 4b.

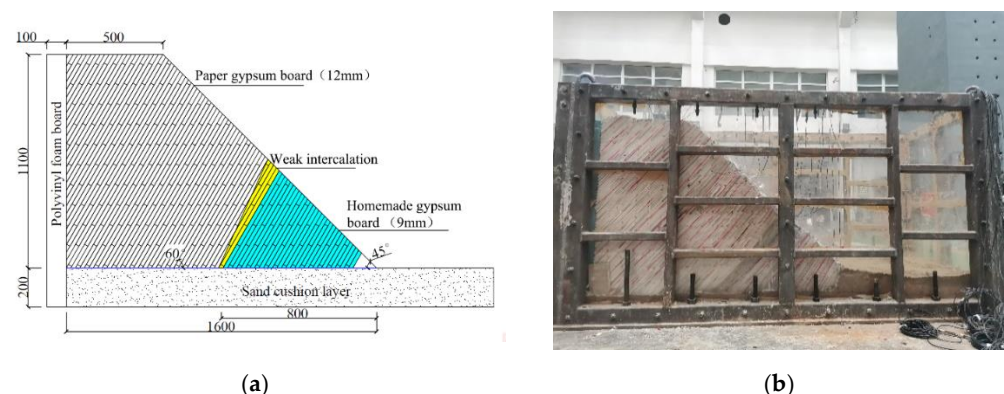


Figure 4. Model test: (a) model design; (b) model masonry drawing.

3.5. Monitoring Alternatives

The test model monitoring device includes twenty-two acceleration sensors, two vibration-pickup devices, and eight displacement devices. All the sensors were arranged on the model’s longitudinal section to reduce the boundary effect on both sides. In the vertical direction inside the slope, five horizontal accelerometers were arranged to study the

dynamic response law. Seven horizontal accelerometers and four vertical accelerometers were arranged from the slope's toe to the slope's top to study the dynamic response of the slope surface. Six horizontal accelerometers were arranged above and below the weak interlayer to study the effect on the dynamic slope response. Two vibration pickup devices were arranged at the top and toe of the slope. Four pull-line-displacement devices were arranged at the top, shoulder, middle, and near the toe of the slope, to monitor the slope settlement under the earthquake action. Four laser displacements were used to record the horizontal displacement of the slope at equal intervals on the slope surface. The specific sensor layout is shown in Figure 5.

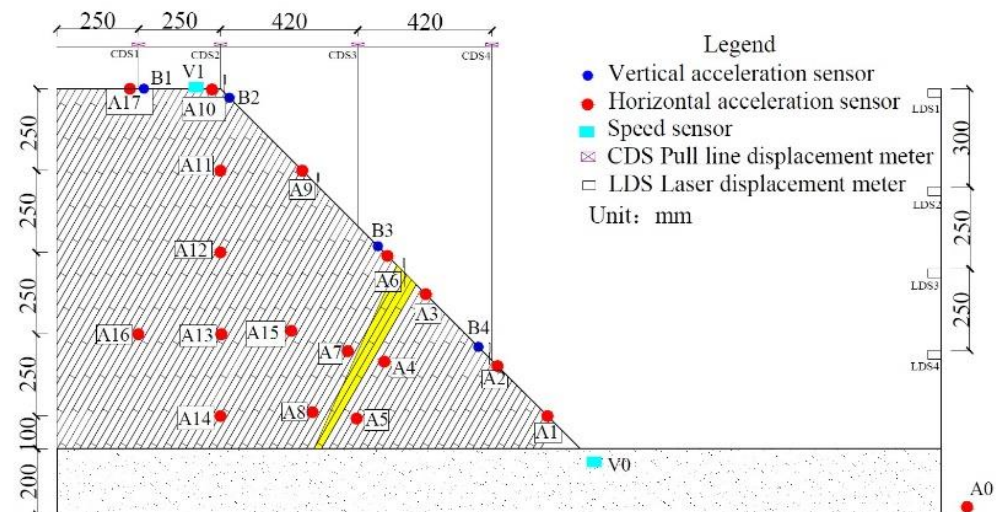


Figure 5. Layout of monitoring points.

3.6. Loading Scheme

To study the effect of ground motion parameters and seismic wave types on the slope dynamic response, the input seismic waves selected in this test were sinusoidal waves, Wenchuan Wolong waves, Wenchuan Maoxian waves, and synthetic waves. To acquire the dynamic characteristics of the slope after each loading, white noise was selected to sweep the slope's frequency. The time history and the Fourier spectrum diagrams of the natural waves are shown in Figures 6 and 7, respectively.

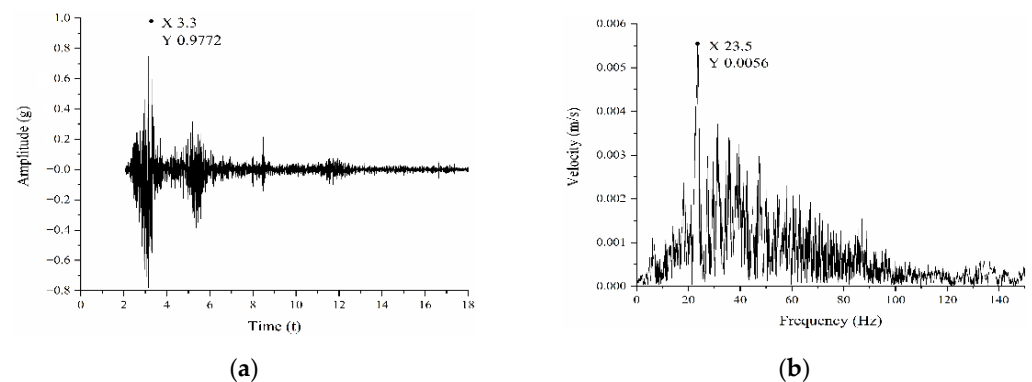


Figure 6. Wolog Earthquake wave in Wenchuan: (a) the time history; (b) the Fourier spectrum.

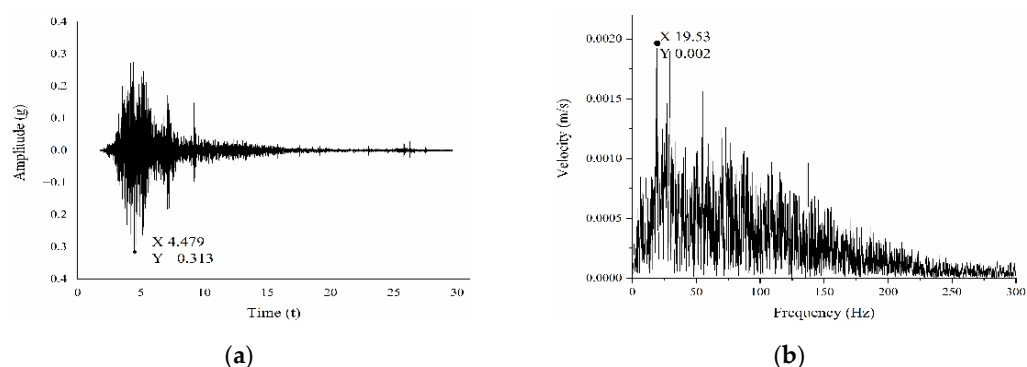


Figure 7. Maoxian Earthquake wave in Wenchuan: (a) the time history; (b) the Fourier spectrum.

Before the seismic waves were loaded, white noise was used to sweep the slope's frequency to obtain its dynamic characteristics. Then, natural waves, sinusoidal waves, and synthetic waves of 0.1 g–0.5 g were applied, with the frequency of sinusoidal waves being 10 Hz–35 Hz, and the interval, 5 Hz. The purpose was to study the influence of the amplitude and frequency and the seismic wave type on the slope's dynamic response. Finally, the amplitude of the inputted natural waves was increased to analyse the slope's failure process under earthquake action. After loading the first amplitude, the test was suspended for 10 min to observe and compare the deformation of the slope and take photographs. It also left enough time for the displacement device to record the displacement of the slope. After the loading of the design loading condition was completed, the slope still did not have an obvious deformation and failure, and a sinusoidal wave with a high amplitude and low frequency was applied until the model had obvious failure. The specific loading schemes are presented in Table 4.

Table 4. Loading scheme.

Loading Sequence	Vibration Characteristics of Shaking Table
1	White noise (denoted as WN1) with an amplitude of 0.1 g
2–7	Sinusoidal wave is loaded in the sequence of excitation frequency 10–35 Hz and interval 5 Hz (hereinafter denoted as $f = 10\text{--}35\text{ Hz}$, $\Delta f = 5\text{ Hz}$) in the X direction of excitation with an amplitude of 0.1 g
8–10	Maoxian wave, Wenchuan wave, and 50-year exceedance probability are 10% (hereinafter denoted as 50–10%), and the amplitude is 0.1 g
11	White noise (denoted as WN2) with an amplitude of 0.1 g
12–17	Sinusoidal wave ($f = 10\text{--}35\text{ Hz}$, $\Delta f = 5\text{ Hz}$), X-direction excitation; the amplitude is 0.2 g
18–21	Maoxian wave, Wenchuan wave, 100–10%, 50–2%; the amplitude is 0.2 g
22	White noise (denoted as WN3) with an amplitude of 0.1 g
23–28	Sinusoidal wave ($f = 10\text{--}35\text{ Hz}$, $\Delta f = 5\text{ Hz}$), X-direction excitation; the amplitude is 0.3 g
29–31	Maoxian wave, Wenchuan wave, 100–2%; the amplitude is 0.3 g and 0.281 g, respectively
32	White noise (denoted as WN4) with an amplitude of 0.1 g
33–38	Sinusoidal wave ($f = 10\text{--}35\text{ Hz}$, $\Delta f = 5\text{ Hz}$), X-direction excitation; the amplitude is 0.4 g
39–41	Maoxian wave, Wenchuan wave, 100–0.1%; the amplitude is 0.4 g
42	White noise (denoted as WN5) with an amplitude of 0.1 g
43–46	Sinusoidal wave ($f = 10\text{--}25\text{ Hz}$, $\Delta f = 5\text{ Hz}$), X-direction excitation; the amplitude is 0.5 g
47–49	Maoxian wave, Wenchuan wave; the amplitude is 0.5 g; white noise (denoted as WN6) with an amplitude of 0.1 g
50–52	Maoxian wave, Wenchuan wave; the amplitude is 0.6 g; white noise (denoted as WN7) with an amplitude of 0.1 g
53–55	Maoxian wave, Wenchuan wave; the amplitude is 0.7 g; white noise (denoted as WN8) with an amplitude of 0.1 g
56–58	Maoxian wave, Wenchuan wave; the amplitude is 0.8 g; white noise (denoted as WN9) with an amplitude of 0.1 g
59–61	Maoxian wave, Wenchuan wave; the amplitude is 0.9 g; white noise (denoted as WN10) with an amplitude of 0.1 g
62–64	Maoxian wave, Wenchuan wave; the amplitude is 1.0 g; white noise (denoted as WN11) with an amplitude of 0.1 g

4. Analysis of Slope Dynamic Characteristics

According to the linear elastic system structure, Xu et al. [47] proposed that the slope's dynamic characteristics include the natural frequency, damping ratio, and vibration mode

of the slope. The dynamic characteristics are a slope's inherent attribute, and it is important to a slope's dynamic response, especially the spectral characteristics. In addition, the change in slope dynamic characteristics also reflects the degree of damage to a slope structure with changes in internal and external factors. The transfer function reflects the transmission characteristics of a system to signals and depends on the characteristics of the system itself, independent of the input [48].

The transfer function is usually solved based on slope acceleration data obtained from white noise excitation in shaking table model tests. Previous scholars have mainly focused on the natural frequency in their analyses of slope characteristics [49], and rarely conducted solution analyses on the damping ratio of a model slope. As an important slope energy-dissipation index parameter, the damping ratio is also of great significance for a slope stability analysis. In this study, based on the monitoring point data obtained by applying white noise excitation in the test process, and using transfer function theory [50], the imaginary part of the relative transfer function of the model slope under white noise excitation at different times was obtained. Meanwhile, to reduce the effect of the shaking table on the slope's dynamic characteristics, the vertical monitoring point (A10–A14) and the table monitoring point (A0) in the slope model were selected. Figure 8 shows the imaginary part of the relative transfer function at the beginning and end of the model. The slope's initial first-order natural frequency was 28.79 Hz. After seismic wave loading under different working conditions, the slope's first-order natural frequency was 21.38 Hz, reduced by 7.41 Hz.

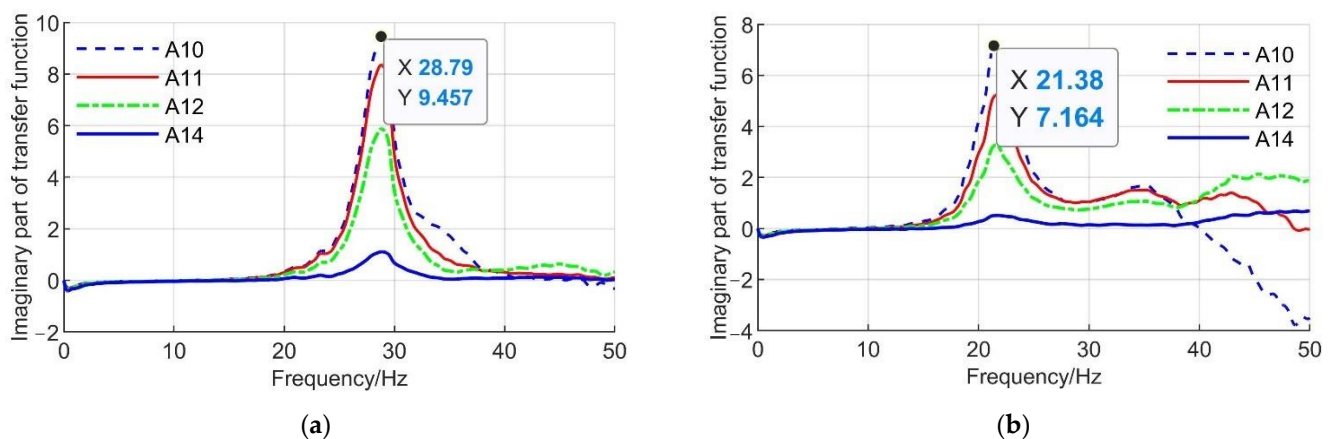


Figure 8. The imaginary part of the relative transfer function of the model slope based on white noise waveform excitation: (a) the first stage; (b) the ending stage.

White noise excitation was used 11 times in the test to obtain the transfer function of the slope under each white noise excitation, using the same method. Figure 9a shows the natural frequency variation of the slope under each white noise excitation. Based on the imaginary part of the relative transfer function of the model slope, the damping ratio of the model slope at different times was calculated using the half-power bandwidth method [50]; the results are shown in Figure 9b. According to the change curves of the natural frequency and damping ratio, the state of the slope under seismic excitation at different times was divided into three stages. The first stage was the linear elastic stage. When the input seismic wave amplitude value was less than 0.3 g, the change in the natural frequencies of the slope was not obvious with the increase in loading, but the damping ratio increased slightly; there were no obvious changes in the model as a whole. The second stage is nonlinear. When the amplitude of the input seismic wave was higher than 0.3 g and less than 0.7 g, the slope's natural frequency dropped sharply, and the damping ratio increased sharply. The slope began to crack, accompanied by a small number of sliding blocks. The third stage is the failure stage. When the input seismic wave exceeded 0.7 g, the slope's natural frequency dropped sharply, and the slope's damping ratio decreased first and then

increased. The slope began to deform appreciably, such as slope-surface block sliding and slope subsidence.

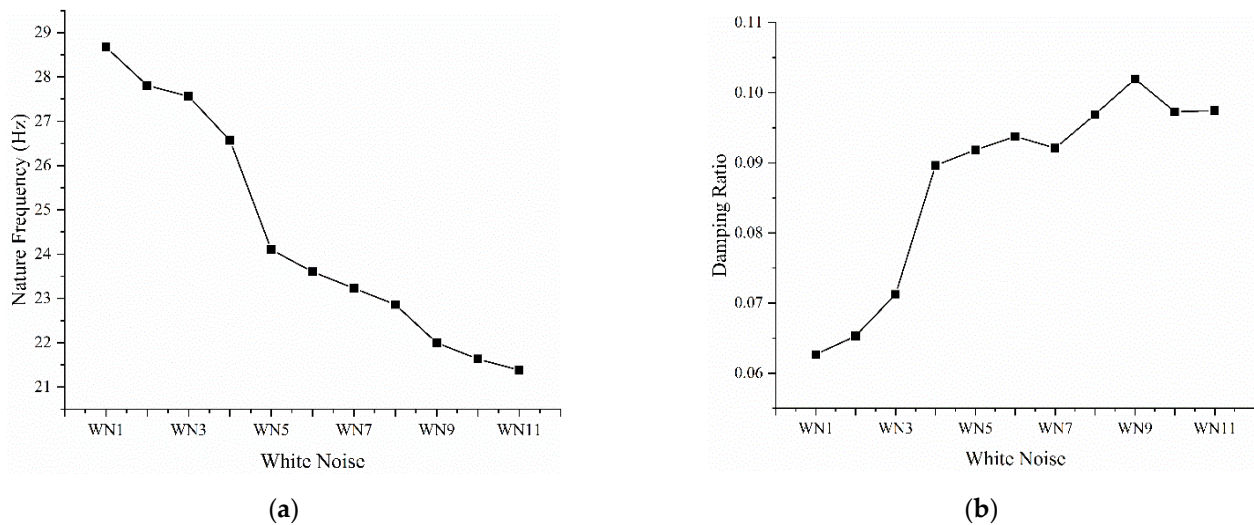


Figure 9. Variation law of slope dynamic characteristics based on white noise excitation: (a) the nature frequencies; (b) the damping ratio.

5. Analysis of Slope Dynamic Response Law and Influencing Factors

5.1. Basic Law of Slope

To study the slope's dynamic response under different seismic action at different stages, the Maoxian wave with amplitudes of 0.2 g and 0.6 g was selected as the dynamic input condition. The slope acceleration amplification factor contour maps are shown in Figure 10, according to the layout of the monitoring points in the slope.

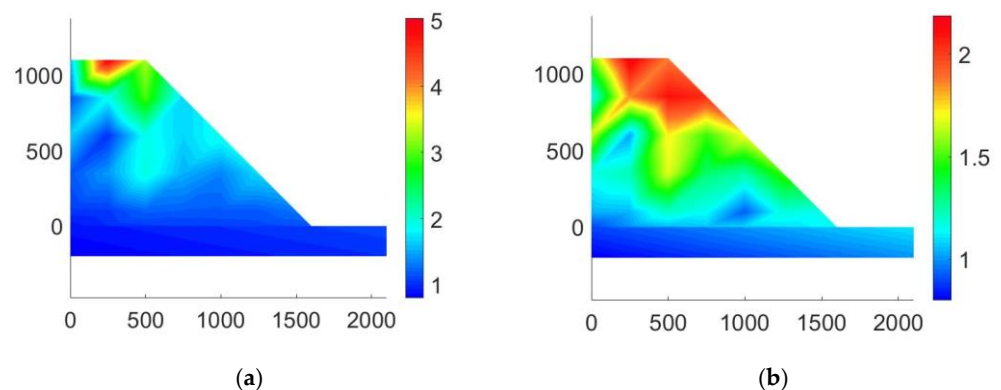


Figure 10. Contour of slope acceleration amplification factor under natural wave action: (a) the 0.2 g Maoxian wave; (b) the 0.6 g Maoxian wave.

Figure 10 shows that the slope had an apparent "elevation effect" under the action of a 0.2 g Maoxian wave and reached a maximum value at the slope's top. Under the action of a 0.6 g Maoxian wave, the range of the elevation amplification effect was wider, with a trend of a sharp increase in the slope's middle. However, the value of the acceleration amplification factor was significantly lower than that under the action of a 0.2 g Maoxian wave. The acceleration amplification factor changed rhythmically along the horizontal direction. The closer to the slope surface, the greater the acceleration amplification factor. With the increase in amplitude and elevation, this "surface effect" became more and more obvious. The variation trends of the slope acceleration amplification factor with elevation are shown in Figure 11, based on the action of seismic waves with different amplitudes.

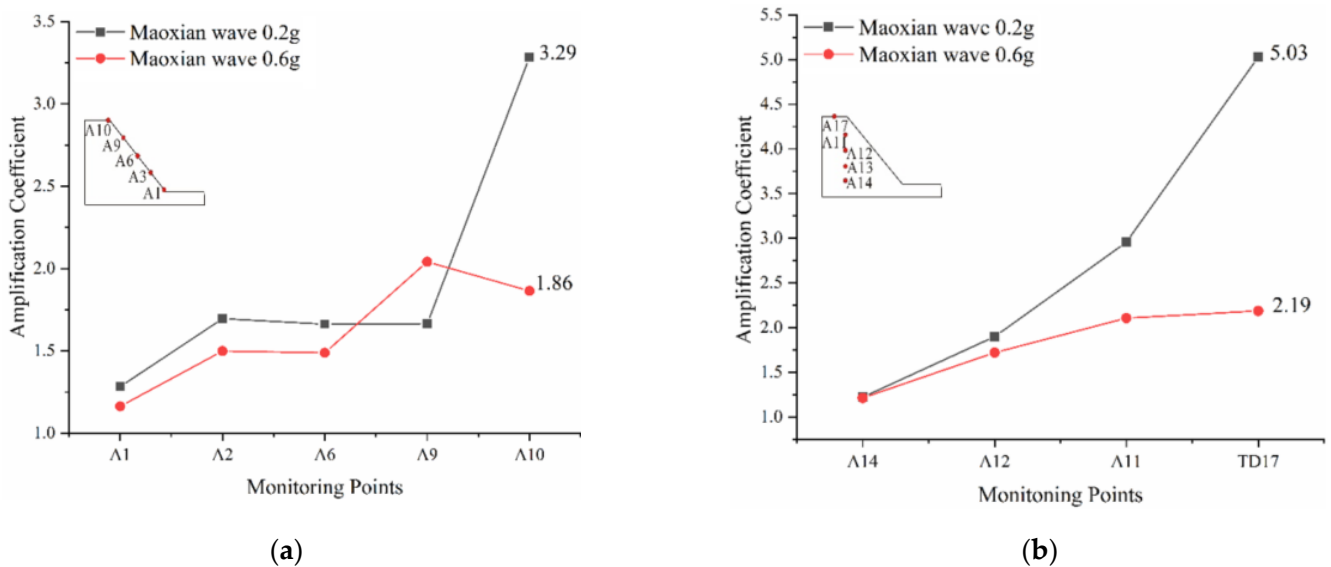


Figure 11. Acceleration amplification factor of the slope under a natural wave: (a) the monitoring points on the slope surface; (b) vertical monitoring points inside the slope.

Figure 11 shows that the acceleration amplification factor changed differently along the slope surface and inside the slope under different amplitudes. Under the action of a 0.2 g sinusoidal wave, the slope acceleration amplification factor increased slowly with the slope-surface height, stayed constant in the slope's middle, then increased sharply from the bottom 3/4 of the slope and reached a maximum at the slope's top. Under the action of a 0.6 g Maoxian wave, the growth trend inside the slope toe was similar to that of the 0.2 g excitation. Still, the acceleration amplification factor appeared to be an obvious inflection point in the slope's middle and reached its maximum value at the elevation 3/4 from the slope's bottom. The vertical acceleration amplification factor inside the slope increased with increasing elevation, showing an apparent elevation amplification effect.

5.2. Influence of Dynamic Parameters

Ground motion parameters have a great influence on slopes' dynamic responses, and a significant amount of research has been conducted in this area (Liu et al., 2014; Liu et al., 2019), but the frequency of the input seismic wave does not exceed the slope's natural frequency. In this study, a sinusoidal wave with an amplitude of 0.3 g and a frequency of 10–35 Hz was applied to determine the effect of the frequency on the slope's dynamic response. A sinusoidal wave with a frequency of 20 Hz and amplitude of 0.1 g–0.5 g was applied to determine the influence of amplitude on the slope's dynamic response. Finally, the effect of the frequency and amplitude on the dynamic slope response was compared and analysed. The data obtained from the slope-surface monitoring points (A1, A3, A6, A9 and A10) and the slope inner monitoring points (A17, A11, A12 and A14) were selected for analysis.

5.2.1. Influence of Frequency

Figure 12 shows the change law of the acceleration amplification factor of the slope surface and inside the slope with different frequencies under the action of a 0.3 g sinusoidal wave.

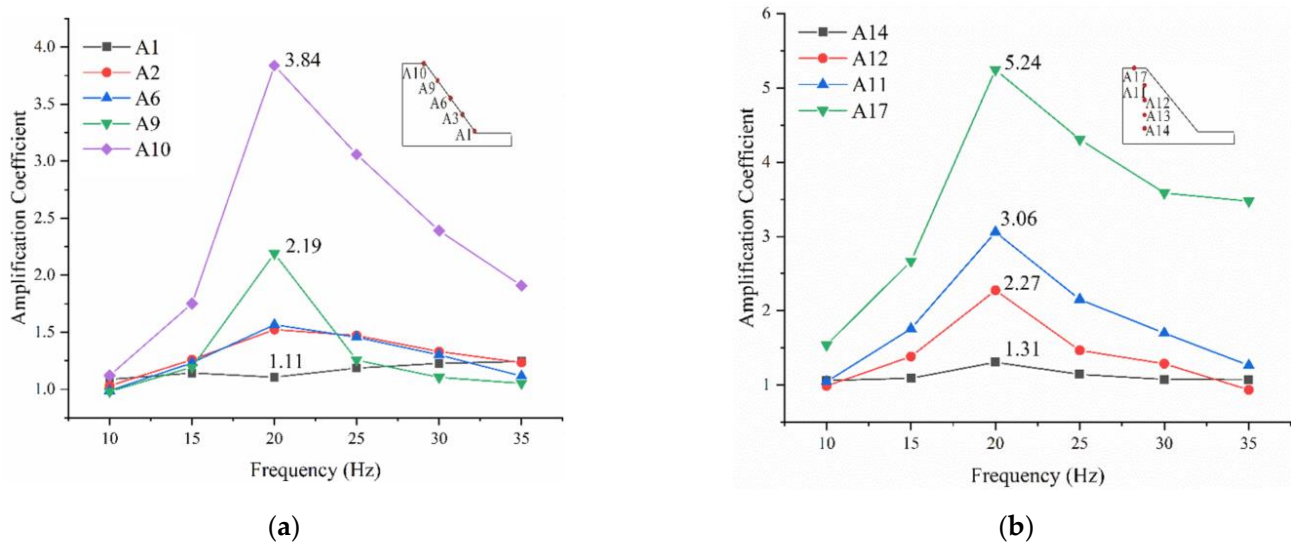


Figure 12. Acceleration amplification factor under different frequencies: (a) the monitoring points on the slope surface; (b) the vertical monitoring points inside the slope.

The acceleration amplification factor first showed a trend of increases, followed by decreases with the rise of input frequency. When the input frequency of a sinusoidal wave was less than 20 Hz, the acceleration amplification factors of the slope surface and inside the slope increased with the increase in input frequency. When the input frequency exceeded 20 Hz, the acceleration amplification factors decreased with the increase in input frequency. This phenomenon was increasingly obvious with the increase in slope height. The acceleration amplification factor of the slope toe did not change noticeably with the increase in input frequency; in some cases, it even weakened the amplification effect of the seismic wave.

Figure 13 shows the variation trend of the acceleration amplification factor with elevation under the action of 0.3 g sinusoidal waves with different frequencies. Under the action of sinusoidal waves of different frequencies, the acceleration amplification factor of slope surface increased nonlinearly with the increase in elevation; the position of the obvious inflection point of the slope acceleration amplification factor was also different. For sinusoidal waves with a frequency of 20 Hz, the acceleration amplification factor increased sharply at 1/2 the slope height, while, for other frequencies, the acceleration amplification factor increased sharply at 3/4 of the slope height. The acceleration amplification factor inside the slope basically showed a linear increase trend with the increase in elevation, with the growth rates being different under the action of different frequencies of sinusoidal waves. The growth rate was the fastest near the natural frequency of the slope.

5.2.2. Influence of Amplitude

It can be seen from Figure 14 that the slope-surface acceleration amplification coefficient first increased and then decreased with an increase in amplitude.

When the input seismic amplitude was less than 0.3 g, the slope-surface acceleration amplification coefficient increased with the increase in amplitude. When the amplitude of the input seismic wave exceeded 0.3 g, it decreased with the increase in the input amplitude, reaching the maximum value at 0.3 g. This is consistent with Liu's et al. [29] conclusion on the influence of amplitude on the dynamic response of the slope, where the slope's acceleration amplification factor first increases and then decreases with the increase in amplitude. However, the corresponding amplitude of the maximum amplification coefficient was higher than her conclusion of 0.2 g. The acceleration amplification factor inside the slope was similar to that of the slope surface, reaching the maximum value when the input sinusoidal wave amplitude was 0.3 g.

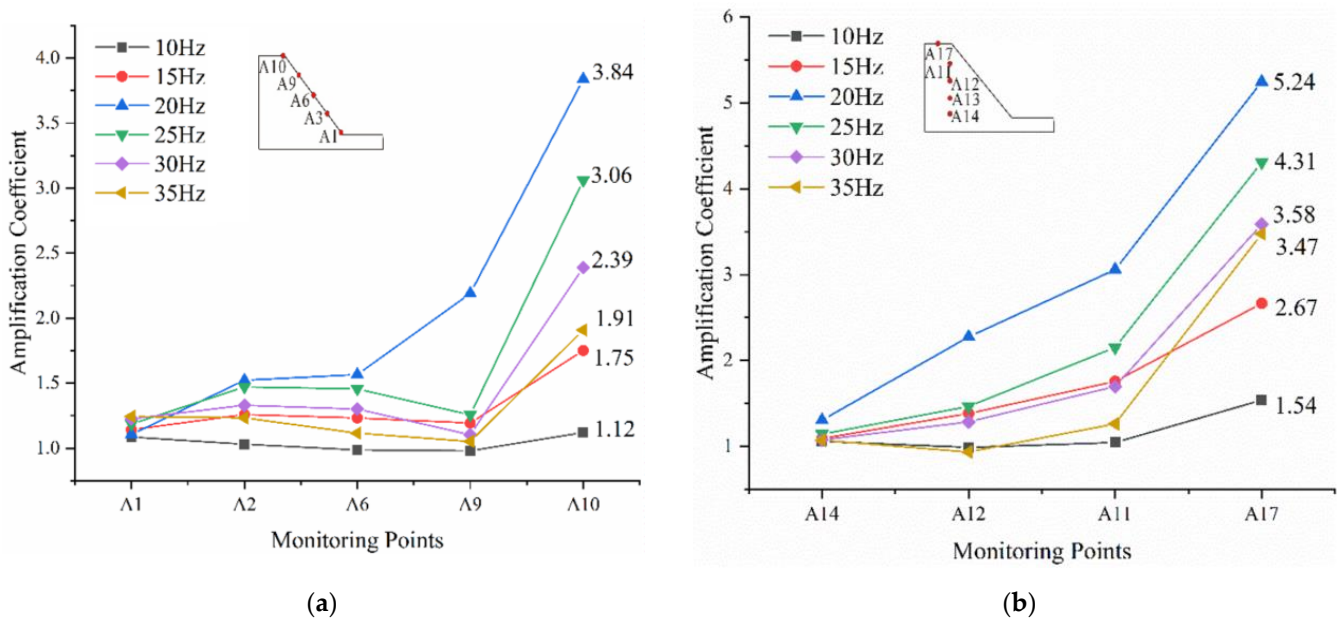


Figure 13. The acceleration amplification factor varies with elevation under different frequencies: (a) the monitoring points on the slope surface; (b) the vertical monitoring points inside the slope.

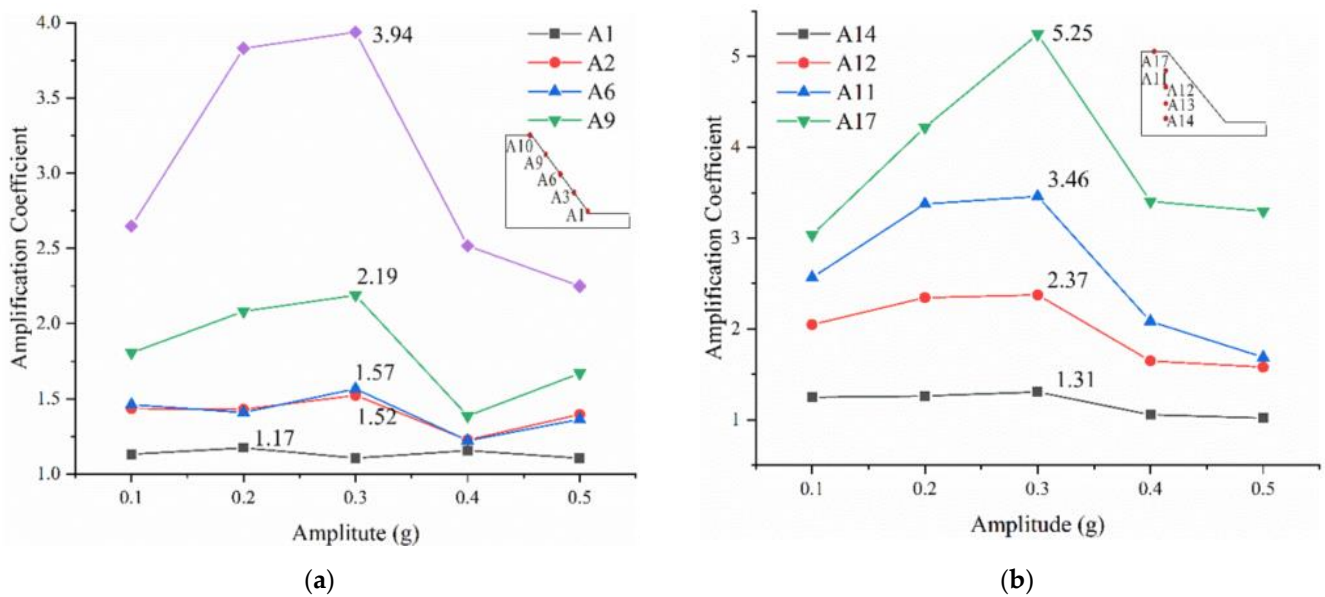


Figure 14. Acceleration amplification factor under different amplitudes: (a) the monitoring points on the slope surface; (b) the vertical monitoring points inside the slope.

Figure 15 shows the change in the slope acceleration amplification factor with elevation under the action of sinusoidal waves with different amplitudes. The slope-surface acceleration amplification factor presented a non-linear increase trend with the increase in elevation. Under the action of different vibration amplitudes, the increase in the position of the acceleration amplification factor was significantly different. When the sinusoidal wave amplitude was less than 0.3 g, the slope grew slowly below 1/2 the slope height, sharply above 1/2 the slope height, and reached the maximum value at the slope’s top. When the sinusoidal wave amplitude was more than 0.3 g, the acceleration amplification factor increased significantly at 3/4 of the slope height. The acceleration amplification factor showed raises linearly along the vertical direction inside the slope, and the change in amplitude had little influence on the increased speed rate of the acceleration amplification factor.

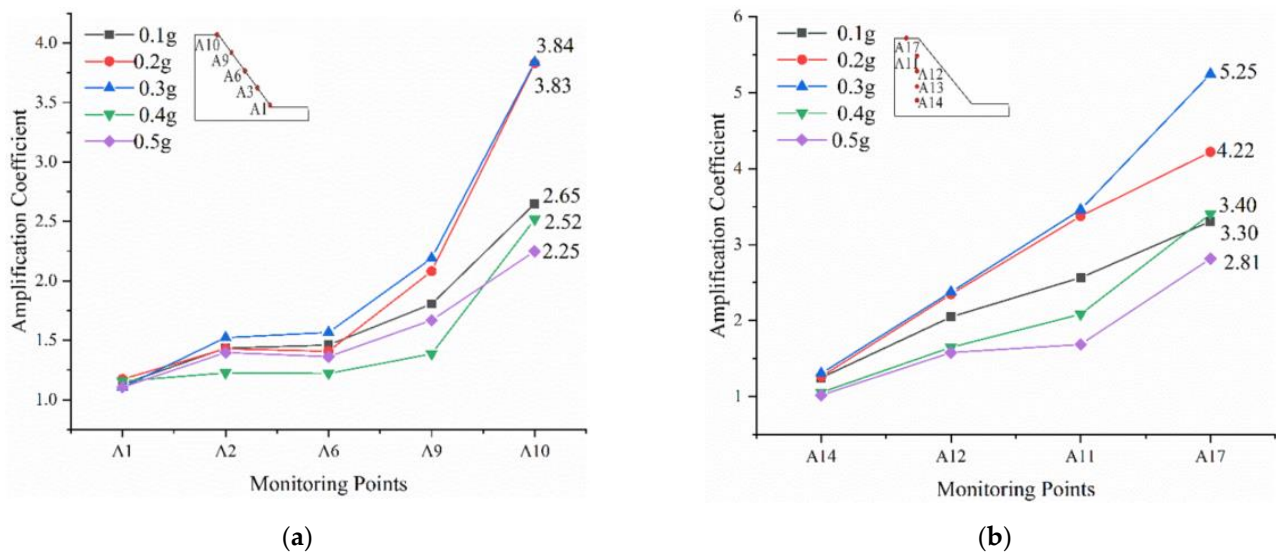


Figure 15. Acceleration amplification factor varies with elevation under different amplitudes: (a) the monitoring points on the slope surface; (b) the vertical monitoring points inside the slope.

Based on the above analysis of the slope's dynamic response, it was found that the frequency and amplitude mutually affect the slope's dynamic response and control the position of the apparent inflection point of the slope-surface acceleration amplification factor. When the input wave was close to the slope's natural frequency or the amplitude was less than 0.3 g, the slope-surface acceleration amplification factor increased sharply in the slope's middle. When the frequency of the input wave was higher or lower than the slope's natural frequency or the amplitude was higher than 0.3 g, the acceleration amplification factor of the slope surface increased sharply at 3/4 of the slope's height. The increasing trend of the vertical acceleration amplification factor inside the slope was less affected by the frequency and amplitude; however, the influence of the input wave frequency on the acceleration amplification factor growth rate was higher than the amplitude. The closer the frequency was to the slope's natural frequency, the faster the acceleration amplification factor curve growth rate.

5.2.3. Influence of Seismic Wave Type

As a type of random wave, seismic waves have complex spectral components, and thus their influence on slopes is different. In this study, the effects of different seismic wave types on the slope's dynamic response were analysed by considering the seismic waves from the bedrock of Maoxian, from the soil layer wave of Wolong, from the synthetic wave based on the study area, and from the sinusoidal wave as the dynamic input conditions. The results are shown in Figure 16.

Figure 16 shows the changes in the acceleration amplification factor of the slope-surface and inside-the-slope monitoring points under the actions of different types of seismic waves. The slope's amplifying effects on the input seismic waves were different for the actions of different types of seismic wave. For the slope-surface monitoring points, except for the slope-shoulder monitoring point, the slope-surface dynamic amplification effects of the natural waves were higher than those of the sinusoidal waves and synthetic waves, and these were higher for the bedrock wave in Maoxian than for the soil layer in Wenchuan. The slope's amplification effect on the synthetic wave was not obvious. Under sinusoidal excitation, the amplification effect of the slope top on the seismic wave was the highest than that for the other seismic waves. For the acceleration amplification factor of the inside of the slope, the amplification effect of the slope on the sinusoidal wave increased gradually with the increase in elevation. The reason for this phenomenon may be related to the input nature frequency and frequency band. As can be seen from Figure 7,

the nature frequency of the bedrock wave in Maoxian was 19.3 Hz, lower than the natural frequency of the slope. However, the frequency band range was between 19.3 and 80 Hz, with a wide frequency band width, resulting in greater energy generated by the slope in the vibration process, so the amplifying effect of the slope was stronger. Although the dominant frequency of the Wenchuan Wolong wave was close to the natural frequency of the slope, and its spectral value was higher than that of the Maoxian wave, its frequency band width was narrow, leading to an insignificant amplifying effect of the slope. Therefore, it is appropriate to select bedrock seismic waves as the input seismic waves for the dynamic study of rock slopes.

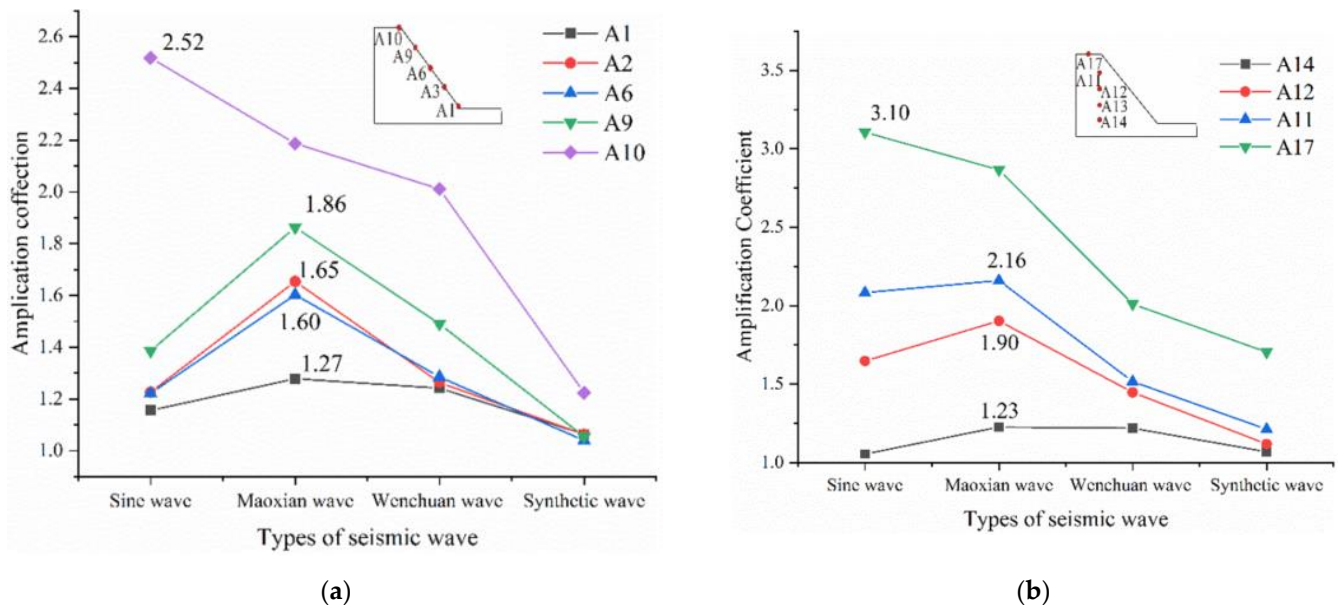


Figure 16. Acceleration amplification factor under different seismic wave types: (a) the monitoring points on the slope surface; (b) the vertical monitoring points inside the slope.

5.2.4. Influence of Structural Plane

The existence of a weakly intercalated layer has a significant influence on the slope's dynamic response. In this study, based on the actual fault, the weakly intercalated layer was designed as a wedge shape. Meanwhile, six accelerometers were arranged above and below the weakly intercalated layer to study the influence of the input seismic wave on the slope's dynamic response. The accelerometers on the upper layer are A6, A7, and A8, and the accelerometers on the lower layer are A3, A4, and A5. The results are shown in Figure 17.

It can be seen from Figure 17 that the amplification effect at different positions was different owing to the inconsistent thickness of the weak interlayer. The weak intercalated layer at the slope's bottom had no obvious effect on the amplification of seismic waves when the input amplitude of the Maoxian wave was 0.2 g. As the elevation increased, the acceleration amplification factor of the upper monitoring points was first higher than that of the lower layer and then lower than that of the lower layer; thus, when the seismic wave passed through the middle of the soft layer, the amplification effect appeared, and the weak intercalated layer at the slope surface inhibited the slope's amplification effect. When the amplitude of the input Maoxian seismic wave was 0.6 g, the amplification effect of the weak intercalated layer at the slope's bottom was obviously enhanced, and in the slope's middle it was weaker than that of the low-amplitude seismic wave; however, near the slope surface, the weak intercalated layer still inhibited the slope's amplification effect on the seismic wave.

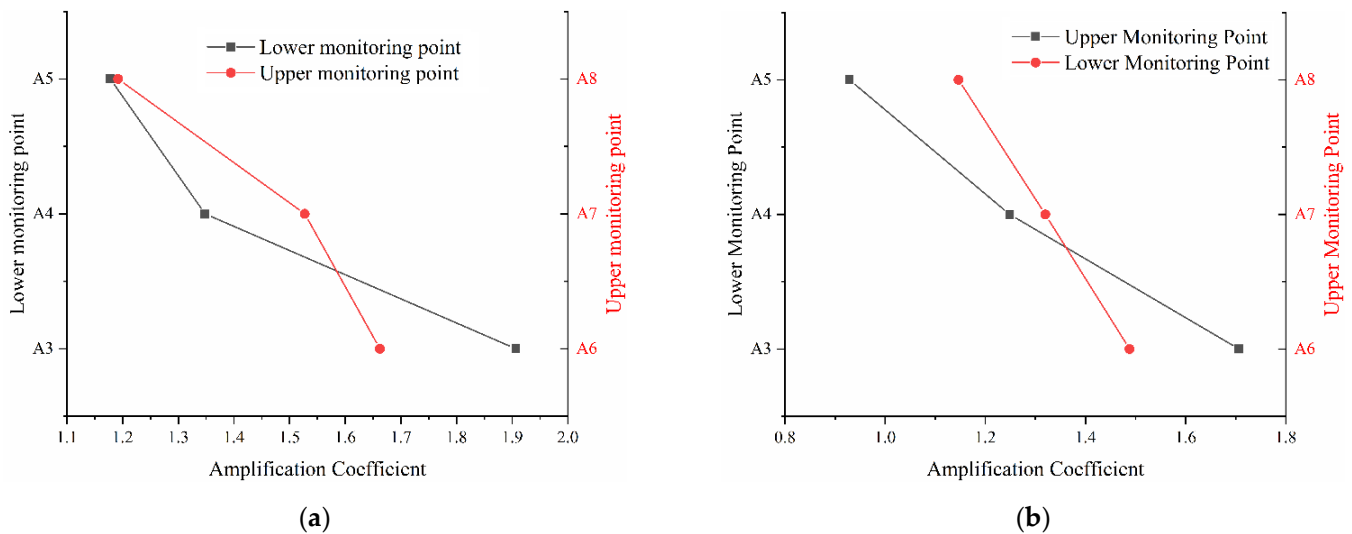


Figure 17. Acceleration amplification factor above and below the weak intercalated layer under different amplitudes: (a) the 0.2 g Maoxian wave; (b) the 0.6 g Maoxian wave.

The Fourier spectrum reflects the spectral properties of ground motion and realises the conversion from the time domain to the frequency domain so that the degree of seismic response in each frequency band and the distribution of ground motion energy in each frequency range can be deeply studied [13]. A fast Fourier transform was used to obtain the Fourier diagram of the measuring points on both sides of the weak intercalated layer under the action of a 0.2 g Maoxian wave and a 0.6 g Maoxian wave. The results are shown in Figure 18.

Figure 18 shows that when the seismic wave passed through the weak intercalated layer from the lower monitoring point to the upper monitoring point, the slope had an apparent amplification effect on the 2–28 Hz frequency band, and this phenomenon became more obvious with the increase in amplitude. When the amplitude of the input Maoxian seismic wave was 0.2 g, the middle of the weak intercalated layer inhibited the seismic waves in low and middle-high frequency bands and amplified the seismic waves in 18–25 Hz bands. When the amplitude of the input Maoxian seismic wave was 0.6 g, the amplification of the seismic wave in the middle of the weak intercalated layer was more obvious in the 36–55 frequency band. The spectral characteristics of the slope were consistent with the variation trend of the acceleration amplification coefficient. For the monitoring points close to the slope surface, the existence of the soft interlayer inhibited the amplification effect of the slope on each frequency band of seismic wave, and the filtering effect on the 18–30 Hz frequency band became more obvious with the increase in amplitude.

Based on the above analysis, it was found that different thicknesses of weak intercalation have different effects on seismic wave propagation in the slope. When the thickness of the weakly intercalated layer was thin, it could amplify the input seismic wave. However, with an increase in the thickness of the weakly intercalated layer, this amplification effect gradually weakened. When the weak intercalated layer exceeded a certain thickness, the slope's amplifying effect on the seismic wave was suppressed, and the phenomenon was affected by the amplitude. The reason for this phenomenon is that when the weak intercalated layer is thin, multiple reflections and refractions occur on the upper and lower layers of the weak structural plane, resulting in the superposition of the seismic waves and the enhancement of the energy of the seismic waves.

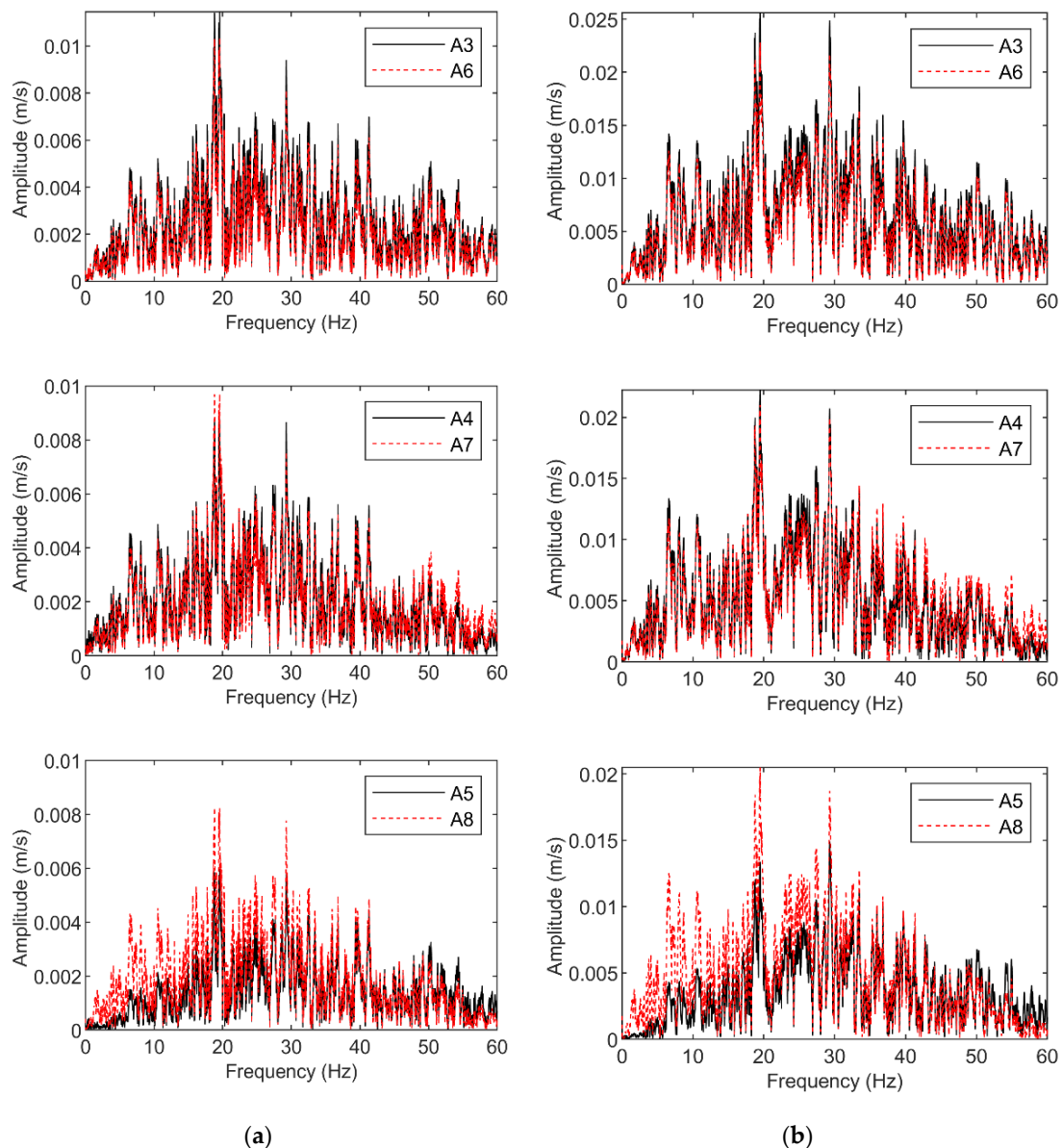


Figure 18. Slope acceleration amplification factor varies with elevation under different amplitudes: (a) the monitoring points on the slope surface; (b) the vertical monitoring points inside the slope.

6. Study on the Slope's Failure Process

During the test, the deformation of the slope was observed for approximately 10 min each time the first seismic wave was loaded, and the deformation was recorded using mobile phones and cameras. The slope's crack development process before the occurrence of overall instability are shown in Figure 19.

When the seismic wave was less than 0.3 g, the slope had no apparent deformation or failure. When the seismic wave reached 0.3 g, transverse tensile cracks and longitudinal cracks appeared at the slope's top, and compression shear microcracks occurred at the slope's toe (Figure 19a,b). When the seismic wave amplitude reached 0.5 g, the transverse tensile cracks extended from the slope's top to the slope's back edge and the slope's shoulder, and the longitudinal cracks at the slope's top connected two transverse tensile cracks (Figure 19c,e). The cracks at the toe of the slope extended further, showing a trend of connecting with each other and developing upward along the slope, and bending deformation occurred on both sides of the toe of the slope (Figure 19d,f). When the amplitude of the seismic wave was 0.6 g–0.7 g, the tensile cracks at the top and middle

of the slope extended to the lower part (Figure 19h); the surface cracks at the toe of the slope developed, and blocks slid on both sides of the slope toe, as well as at the shoulder and middle of the slope (Figure 19g). When the seismic wave amplitude reached 0.8 g, the block at the slope's toe formed a penetrating crack, the block slipped, the soft structural plane bent and broke, and a large number of slope-surface blocks slid and accumulated at the slope's toe, resulting in a river-blocking disaster (Figure 19i). At the same time, shear cracks at the slope's toe further developed upward. Under the action of seismic waves (0.9 g–1.0 g), blocks at the slope's toe slipped to form a temporary surface, resulting in bending deformation at the slope's upper part. In the slope, the upper tensile cracks and the lower shear cracks formed a transfixing sliding surface, the main sliding surface was formed, and slope instability failure occurred (Figure 19j).

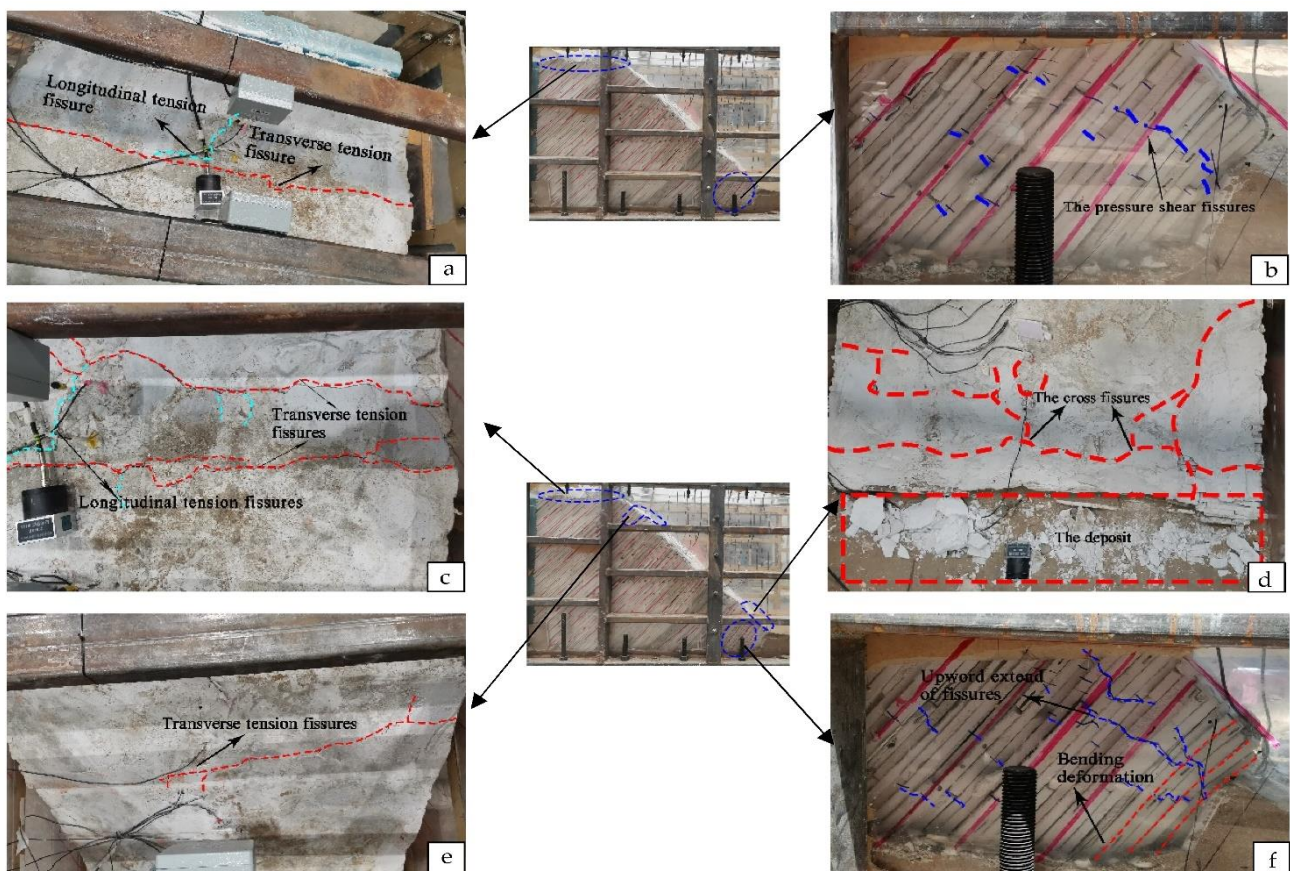


Figure 19. Cont.

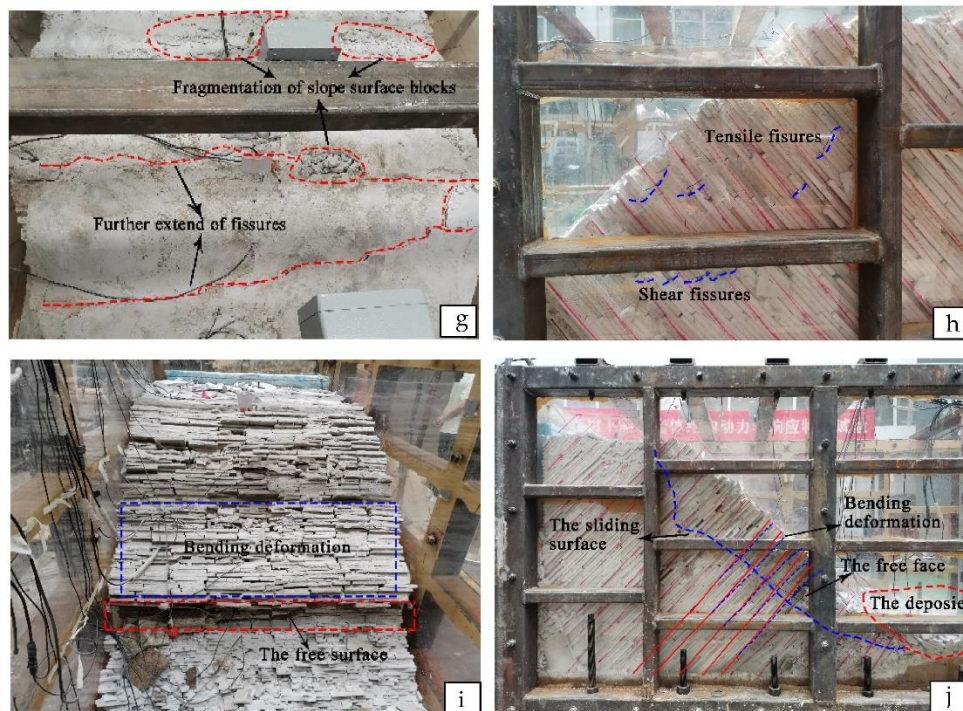


Figure 19. Failure process of slope: (a) crack at the top of the slope; (b) pressure shear crack at slope toe; (c) crack extension at the top of the slope; (d) slip block; (e) tensile crack of slope shoulder; (f) the pressure shear cracks are interpenetrating each other on the slope toe; (g) block fragmentation and tensile fracture extension; (h) compression shear crack and tension crack are partially connected; (i) the block slips and bending deformation occurs above the slope; (j) the main slip surface is formed.

According to the slope's instability failure process under the action of seismic waves with different amplitudes, it was found that 0.3 g was the critical dynamic condition for the initiation of slope cracks. When the seismic amplitude was greater than 0.3 g, tensile cracks occurred at the slope's top and slope's middle, and compression shear cracks occurred at the slope's toe. The fragmentation degree of the slope-surface blocks increased with an increase in the amplitude. The slope entered the nonlinear stage from the linear stage, with 0.8 g being the critical dynamic condition for slope failure. At that time, the surface block of the slope slid, and the compression-shear crack at the toe of the slope was connected and developed upward. In addition, the tension crack at the top developed toward the interior of the slope, forming the main sliding surface with a compression-shear crack at the bottom. With the increase in amplitude, many sliding blocks occurred at the slope's toe and accumulated there. The formed free face led to the bending deformation of the upper block and bending of the inner block, resulting in the slope being in a state of instability failure.

7. Conclusions

1. The slope has an obvious "elevation effect" and "surface effect", and the distribution range of the slope dynamic amplification effect is different under different amplitudes. The acceleration amplification factors of the slope surface and inside the slope show different increasing trends with elevation. The acceleration amplification factor of the inside slope increases linearly with an increase in elevation. However, the acceleration amplification factor of the slope surface increases slowly at first and then sharply with elevation, and the position of the obvious increase is controlled by the frequency and amplitude of the input wave. When the frequency of the input wave is close to the natural frequency of the slope or the amplitude is less than 0.3 g, the acceleration amplification factor of the slope surface increases sharply at the position of 1/2 the

- slope height, and increases sharply at the position of 3/4 of the slope height under the action of other input waves.
2. The ground motion parameters have different effects on the slope's dynamic response. The acceleration amplification factor of the slope first increases and then decreases with an increase in frequency, and the inflection point of the acceleration amplification factor is affected by the amplitude. When the input seismic wave frequency is near the natural frequency of the slope, the acceleration amplification factor of the slope increases first and then decreases with an increase in the input amplitude, and the amplitudes corresponding to the maximum acceleration amplification factors inside the slope and at the slope surface are different. Frequency affects the acceleration amplification growth rate of the slope, which is more obvious for the monitoring points inside the slope. The closer to the natural frequency of the slope, the faster the acceleration amplification factor curve increases. The amplitude has little effect on the rate of increase in the slope acceleration amplification factor.
 3. The amplification effect of the slope on different input waves was different. The amplification effect of the rocky slope on the input bedrock seismic waves is higher than that of the input soil seismic waves, but the amplification effect of the slope top on the sinusoidal waves is obviously higher than that of other types of input waves. Therefore, in shaking table tests, bedrock seismic waves should be used for rock slopes, and soil seismic waves should be used for soil slopes.
 4. The weak intercalated layer has no obvious effect on the change in the seismic wave spectrum; it shows good symmetry under different amplitudes. However, it can amplify or suppress the seismic wave energy, owing to the influence of the thickness of the soft structural plane. When the thickness of the weak section is low, the input seismic wave can be amplified. With an increase in the thickness of the soft structural plane, the amplification effect of the seismic wave is gradually weakened and even suppressed.
 5. The slope's failure process can be roughly divided into three stages: (1) the formation of tensile cracks at the top and shear cracks at the toe; (2) the extension of cracks and the sliding of the slope-surface block; (3) the formation of the main sliding surface. The critical dynamic condition for slope fracture initiation is 0.3 g, and 0.8 g is the critical dynamic condition for slope failure.

Author Contributions: The paper was written by K.-S.G. under the guidance of M.-Z.G. The project administration was carried out by C.W. The data curation and methodology were proposed by K.-S.G. All authors have read and agreed to the published version of the manuscript.

Funding: This research is financially supported by the National Key Research and Development Project of China (Grant No. 2018YFC1505001).

Institutional Review Board Statement: Not applicable.

Informed Consent Statement: Informed consent was obtained from all subjects involved in the study. Written informed consent has been obtained from the patient(s) to publish this paper.

Data Availability Statement: The data presented in this study are available on request from the corresponding author. The data are not publicly available due to the test data will be collected and submitted to the National Data Center for Qinghai-Tibet Plateau Science.

Conflicts of Interest: The authors declare no conflict of interest.

References

1. Dai, F.C.; Deng, J.H. Development characteristics of landslide hazards in Three-rivers basin of Southeast Tibetan plateau. *Adv. Eng. Sci.* **2020**, *52*, 3–15.
2. Li, S.; Chen, J.B.; Yao, Y.; Wu, G.D.; Xie, J.L. Risk analysis on seismic landslides by GIS: Take Yili area as an example. *Inland Earthq.* **2021**, *35*, 38–47.
3. Yin, Y.P. Features of landslides triggered by the Wenchuan earthquake. *J. Eng. Geol.* **2009**, *17*, 29–38.
4. Chigira, M.; Wu, X.Y.; Inokuc, T.; Wang, G.H. Landslides induced by the 2008 Wenchuan earthquake, Sichuan, China. *Geomorphology* **2010**, *118*, 225–238. [[CrossRef](#)]

5. Li, G.; Hua, H.L.; Zhao, J.J. Spectrum characteristics of stratified rock slopes using shaking table test. *J. Eng. Geol.* **2016**, *24*, 959–966.
6. Froude, M.J.; Petley, D.N. Global fatal landslide occurrence from 2004 to 2016. *Nat. Hazards Earth Syst. Sci.* **2018**, *18*, 2161–2181. [[CrossRef](#)]
7. Chen, J.; Cui, Z.J. Discovery of outburst deposits induced by the Xuelongnang paleo landslide-dammed lake in the upper Jinsha river, China and its environmental and hazard significance. *Acta Sedimentol. Sin.* **2015**, *33*, 275–284.
8. Huang, R.Q.; Pei, X.J.; Fan, X.M.; Zhang, W.F.; Li, S.G.; Li, B.L. The characteristics and failure mechanism of the largest landslide triggered by the Wenchuan earthquake, May 12, 2008, China. *Landslides* **2012**, *1*, 131–142. [[CrossRef](#)]
9. Sepulveda, S.A.; Murphy, W.; Jibson, R.W.; Petley, D.N. Seismically induced rock slope failures resulting from topographic amplification of strong ground motions: The case of Pacoima Canyon, California. *Eng. Geol.* **2005**, *80*, 336–348. [[CrossRef](#)]
10. Ma, N.; Wang, G.; Kamai, T.; Doi, I.; Chigira, M. Amplification of seismic response of a large deep-seated landslide in Tokushima, Japan. *Eng. Geol.* **2019**, *249*, 218–234. [[CrossRef](#)]
11. Shen, T.; Wang, Y.S.; Luo, Y.H.; Xin, C.C.; Liu, Y. Seismic response of cracking features in Jubao Mountain during the aftershocks of Jiuzhaigou Ms7.0 earthquake. *J. Mt. Sci.* **2019**, *16*, 2532–2547. [[CrossRef](#)]
12. Hu, X.L.; Wang, Y.S.; Liu, J.; Liu, Y.; Shen, T.; Xin, C.C. Analysis of ground motion response monitoring data of Xuejiaba site of Ms 4.1 aftershock in Jiuzhaigou. *Sci. Technol. Eng.* **2019**, *19*, 49–55.
13. Wang, Y.S.; He, J.X.; Luo, Y.H.; Hao, Z.H.; Liu, Y.; Zhang, L. Seismic responses of Lengzhuguan slope during Kangding Ms5.8 earthquake. *J. Southwest Jiaotong Univ.* **2015**, *50*, 838–844. [[CrossRef](#)]
14. Wasowski, J.; Gaudio, V.D. Evaluating seismically induced mass movement hazard in Caramanico Terme (Italy). *Eng. Geol.* **2000**, *58*, 291–311. [[CrossRef](#)]
15. Li, H.B.; Liu, Y.Q.; Liu, L.B.; Liu, B.; Xia, X. Numerical evaluation of topographic effects on seismic response of single-faced rock slopes. *Bull. Eng. Geol. Environ.* **2017**, *78*, 1873–1891. [[CrossRef](#)]
16. He, J.X.; Qi, S.W.; Wang, Y.S.; Saroglou, C. Seismic response of the Lengzhuguan slope caused by topographic and geological effects. *Eng. Geol.* **2020**, *265*, 105431. [[CrossRef](#)]
17. Wang, T.; Gao, C.L.; Huang, F.; Peng, D.; Tian, S.W.; Li, H.L. Dynamic response of rock slope with anti-dip weak intercalated layer and its influencing factors under seismic actions. *Arab. J. Geosci.* **2021**, *14*, 425. [[CrossRef](#)]
18. Shi, G.X.; Guang, C.Z.; Jing, K.L. Laws of influence upon dynamic response of high rock slope by seismic wave frequency. *Appl. Mech. Mater.* **2012**, *170*, 615–625.
19. Song, D.Q.; Che, A.L.; Zhu, R.J.; Ge, X.R. Natural frequency characteristics of rock masses containing a complex geological structure and their effects on the dynamic stability of slopes. *Rock Mech. Rock Eng.* **2019**, *52*, 4457–4473. [[CrossRef](#)]
20. Song, D.Q.; Huang, J.; Liu, X.L. Dynamic response of layered rock slopes under earthquakes. *J. Hunan Univ. (Nat. Sci. Ed.)* **2021**, *48*, 113–120.
21. Feng, X.X.; Jiang, Q.H.; Zhang, H.C.; Zhang, X.B. Study on the dynamic response of dip bedded rock slope using discontinuous deformation analysis (DDA) and shaking table tests. *Int. J. Numer. Anal. Methods Geomech.* **2020**, *45*, 411–427. [[CrossRef](#)]
22. Mao, L.J.; Xu, Q.; Zheng, J.; Zhu, Y. Dynamic Responses of slope under the effect of seismic loads. *Appl. Mech. Mater.* **2013**, *438*, 1587–1591. [[CrossRef](#)]
23. Zhao, L.Y.; Huang, Y.; Hu, H.Q. Stochastic seismic response of a slope based on large-scale shaking-table tests. *Eng. Geol.* **2020**, *277*, 105782. [[CrossRef](#)]
24. Srilatha, N.; Madhavi Latha, G.; Puttappa, C.G. Effect of frequency on seismic response of reinforced soil slopes in shaking table tests. *Geotext. Geomembr.* **2013**, *36*, 27–32. [[CrossRef](#)]
25. Feng, X.X.; Jiang, Q.H.; Zhang, X.B.; Zhang, H.C. Shaking table model test on the dynamic response of anti-dip rock slope. *Geotech. Geol. Eng.* **2019**, *37*, 1211–1221. [[CrossRef](#)]
26. Zhou, Z.J.; Fan, Y.L.; Yan, K.F. Shaking table model test of slope seismic dynamic response. *J. High. Transp. Res. Dev. Engl. Ed.* **2017**, *11*, 23–32. [[CrossRef](#)]
27. Liu, H.X.; Xu, Q.; Wang, L.; Hou, H.J. Effect of frequency of seismic wave on acceleration response of rock slopes. *Chin. J. Rock Mech. Eng.* **2014**, *33*, 125–133.
28. Chen, C.C.; Li, H.H.; Chiu, Y.C.; Tsai, Y.K. Dynamic response of a physical anti-dip rock slope model revealed by shaking table tests. *Eng. Geol.* **2020**, *277*, 105772. [[CrossRef](#)]
29. Liu, H.X.; Xu, Q.; Li, Y.R.; Fan, X.M. Response of high-strength rock slope to seismic waves in a shaking table test. *Bull. Seismol. Soc. Am.* **2013**, *103*, 3012–3025. [[CrossRef](#)]
30. Yang, G.X.; Qi, S.W.; Wu, F.Q.; Zhan, Z.F. Seismic amplification of the anti-dip rock slope and deformation characteristics: A large-scale shaking table test. *Soil Dyn. Earthq. Eng.* **2018**, *115*, 907–916. [[CrossRef](#)]
31. Chen, Z.L.; Hu, X.; Xu, Q. Experimental study of motion characteristics of rock slopes with weak intercalation under seismic excitation. *J. Mt. Sci.* **2016**, *13*, 546–556. [[CrossRef](#)]
32. Li, H.H.; Lin, C.H.; Zu, W.; Chen, C.C.; Weng, M.C. Dynamic response of a dip slope with multi-slip planes revealed by shaking table tests. *Landslides* **2018**, *15*, 1731–1743. [[CrossRef](#)]
33. He, J.X.; Qi, S.W.; Zhan, Z.F.; Guo, S.F.; Li, C.L.; Zheng, B.W.; Huang, X.L.; Zou, Y.; Yang, G.X.; Liang, N. Seismic response characteristics and deformation evolution of the bedding rock slope using a large-scale shaking table. *Landslides* **2021**, *18*, 2835–2853. [[CrossRef](#)]

34. Li, M.L.; Wang, K.L. Seismic slope behavior in a large-scale shaking table model test. *Eng. Geol.* **2006**, *86*, 118–133.
35. Fan, G.; Zhang, J.J.; Wu, J.B.; Yan, K.M. Dynamic Response and dynamic failure mode of a weak intercalated rock slope using a shaking table. *Rock Mech. Rock Eng.* **2016**, *49*, 3243–3256. [[CrossRef](#)]
36. Li, L.Q.; Ju, N.P.; Zhang, S.X.; Deng, X.X. Shaking table test to assess seismic response differences between steep bedding and toppling rock slopes. *Bull. Eng. Geol. Environ.* **2019**, *78*, 519–531. [[CrossRef](#)]
37. Deng, Z.Y.; Liu, X.R.; Liu, Y.Q.; Liu, S.L.; Han, Y.F.; Liu, J.H.; Tu, Y.L. Model test and numerical simulation on the dynamic stability of the bedding rock slope under frequent microseisms. *Earthq. Eng. Eng. Vib.* **2020**, *19*, 919–935. [[CrossRef](#)]
38. Wang, K.L.; Lin, M.L. Initiation and displacement of landslide induced by earthquake—A study of shaking table model slope test. *Eng. Geol.* **2011**, *122*, 106–114. [[CrossRef](#)]
39. Huang, D.; Ma, H.; Meng, Q.J.; Song, Y.X. Centrifugal model test and numerical simulation for anacinal rock slopes with soft-hard interbedded structures. *Chin. J. Geotech. Eng.* **2020**, *42*, 1286–1295.
40. Huang, D.; Xie, Z.Z.; Song, Y.X.; Meng, Q.J.; Luo, S.L. Centrifuge model test study on the toppling deformation of the anti-dip soft-hard interbedded rock slopes. *Chin. J. Rock Mech. Eng.* **2021**, *40*, 1357–1368.
41. Li, Y.Q.; Huang, D.; Meng, Q.J. An analysis of the deformation characteristics of soft-hard interbedded anti-tilting layered rock slope based on centrifuge and numerical simulation. *Hydrogeol. Eng. Geol.* **2021**, *48*, 141–150.
42. Li, S.J.; Sun, Q.C.; Zhang, Z.H.; Luo, X.Q. Physical modelling and numerical analysis of slope instability subjected to reservoir impoundment of the Three Gorges. *Environ. Earth Sci.* **2018**, *77*, 138–154. [[CrossRef](#)]
43. Paster, M.; Martin Stickle, M.; Dutto, P.; Mira, P.; Fernández Merodo, J.A.; Blanc, T.; Sancho, S.; Benítez, A.S. A viscoplastic approach to the behaviour of fluidized geomaterials with application to fast landslides. *Contin. Mech. Thermodyn.* **2015**, *27*, 21–47. [[CrossRef](#)]
44. Paster, M.; Blanc, T.; Haddad, B.; Petrone, S.; Sanchez Morles, M.; Drempevic, V.; Issler, D.; Crosta, G.B.; Cascini, L.; Sorbino, G.; et al. Application of a SPH depth-integrated model to landslide run-out analysis. *Landslides* **2014**, *11*, 793–812. [[CrossRef](#)]
45. Kakogiannou, E.; Sanavia, L.; Nicot, F.; Darve, F.; Schrefler, B.A. A porous media finite element approach for soil instability including the second-order work criterion. *Acta Geotech.* **2016**, *11*, 805–825. [[CrossRef](#)]
46. Sosio, R.; Giovanni, B.C.; Hungr, O. Complete dynamic modeling calibration for the Thurwieser rock avalanche (Italian Central Alps). *Eng. Geol.* **2008**, *100*, 11–26. [[CrossRef](#)]
47. Xu, G.X.; Yao, L.K.; Gao, Z.N.; Li, Z.H. Large-scale shaking table model test study on dynamic characteristics and dynamic responses of slope. *Chin. J. Rock Mech. Eng.* **2008**, *27*, 624–632.
48. Zhou, Z.P.; Huang, H.; Li, L.Q.; Huang, H.P.; Wei, H.B. Application study of transfer function in vibrating detection. *Electron. Meas. Technol.* **2018**, *41*, 126–130.
49. Fan, G.; Zhang, J.J.; Fu, X.; Wang, M.Y. Application of transfer function to on-site shaking table test. *Rock Soil Mech.* **2016**, *37*, 2869–2876.
50. Jiang, L.W.; Yao, L.K.; Wu, W.; Xu, G.X. Transfer function analysis of earthquake simulation shaking table model test of side slopes. *Rock Soil Mech.* **2010**, *31*, 1368–1374.